Astron. Astrophys. 359, 51–64 (2000)

ASTRONOMY AND ASTROPHYSICS

Deep far infrared ISOPHOT survey in "Selected Area 57"

I. Observations and source counts

M.J.D. Linden-Vørnle[1,2], H.U. Nørgaard-Nielsen[2], H.E. Jørgensen[1], L. Hansen[1], M. Haas[3], U. Klaas[3], P. Ábrahám[3], D. Lemke[3], I. Lundgaard Rasmussen[2], and H.W. Schnopper[4]

[1] Niels Bohr Institute for Astronomy, Physics and Geophysics, Astronomical Observatory, Juliane Maries Vej 30, 2100 København Ø, Denmark
[2] Danish Space Research Institute, Juliane Maries Vej 30, 2100 København Ø, Denmark
[3] Max-Planck-Institut für Astronomie (MPIA), Königstuhl 17, 69117 Heidelberg, Germany
[4] Harvard-Smithsonian Center for Astrophysics, 60 Garden Street, Cambridge, MA 02138, USA

Received 29 October 1999 / Accepted 26 April 2000

Abstract. We present here the results of a deep survey in a 0.4 deg^2 blank field in Selected Area 57 conducted with the ISOPHOT instrument aboard ESAs Infrared Space Observatory (ISO[1]) at both 60 μm and 90 μm. The resulting sky maps have a spatial resolution of 15 $\times$ 23 arcsrc^2 per pixel which is much higher than the 90 $\times$ 90 arcsec^2 pixels of the IRAS All Sky Survey. We describe the main instrumental effects encountered in our data, outline our data reduction and analysis scheme and present astrometry and photometry of the detected point sources. With a formal signal to noise ratio of 6.75 we have source detection limits of 90 mJy at 60 μm and 50 mJy at 90 μm. To these limits we find cumulated number densities of 5 ± 3.5 deg^{-2} at 60 μm and 14.8 ± 5.0 deg^{-2} at 90 μm. These number densities of sources are found to be lower than previously reported results from ISO but the data do not allow us to discriminate between no-evolution scenarios and various evolutionary models.

Key words: infrared: galaxies – galaxies: evolution – galaxies: starburst

1. Introduction

It is widely accepted that a significant part of the evolution of galaxies is hidden from UV/optical studies due to internal absorption by dust grains, and that the absorbed radiation is re-emitted in the infrared.

The IRAS All Sky Survey has revealed more than 25.000 galaxies, of which only half were already known at optical wavelengths (Soifer et al. 1987). The vast majority of these are local late-type spirals while ellipticals and S0 galaxies were rarely detected. Only a few very luminous infrared galaxies were detected at significant redshifts.

A first indication of a possible evolution of the population of infrared sources at the IRAS detection limit was found by Hacking & Houck (1987) (HH87 hereafter). They exploited all the data obtained during observations of the IRAS secondary calibration source, NGC 6543, a planetary nebula close to the North Ecliptic Pole. Although this area (6.25 deg^2) is far from being the most 'cirrus clean' area in the sky, the extensive coverage by IRAS resulted in detection of sources (S/N > 5) down to about 50 mJy in the 60 μm band, about 10 times fainter than the detection limit in the IRAS All Sky Survey.

Following the pioneering work by HH87 several other deep IRAS surveys have been published. Gregorich et al. (1995) have analysed ~ 20 deg^2 – socalled filler fields, not including the HH87 field – with eight or more observations and designated with 'moderate cirrus' or 'low cirrus' flags in the IRAS Faint Source Survey (FSS) (Moshir et al. 1992). Gregorich et al. (1995) find the source density at $f_\nu(60\,\mu\mathrm{m}) = 50$ mJy to be about twice as high as that found by HH87.

Bertin et al. (1997) have extracted 60 μm data from the FSS from ~ 400 deg^2 in four separate contiguous areas selected with good coverage, low cirrus indicators and a minimum of nearby galaxies. They have performed a detailed analysis of the statistical errors in the number counts at the faint limit – the Eddington bias – and give corrected number counts down to $f_\nu(60\,\mu\mathrm{m}) = 100$ mJy. At this limit they find a source density about 25% lower than HH87. They suggest that the large discrepancy between their results and Gregorich et al. (1995) is caused by cirrus contamination in their fields.

Analysing the HH87 data, Hacking et al. (1987) found a significant excess of their 60 μm number density below 100 mJy, if no evolution out to $z \approx 0.2$ is assumed. They fit the number densities with simple models assuming a power law in $(1+z)$ either as pure density or pure luminosity evolution, but are not able to distinguish between these two types of models.

This excess of sources at faint infrared fluxes have invoked a considerable effort in constructing theoretical models for galaxy

Send offprint requests to: M.J.D. Linden-Vørnle (michael@astro.ku.dk)

[1] Based on observations with ISO, an ESA project with instruments funded by ESA member states (especially the PI countries: France, Germany, the Netherlands, and the United Kingdom) and with the participation of ISAS and NASA.

evolution. Guiderdoni et al. (1998) present semi-analytic models of galaxy evolution in the infrared following the non-dissipative and dissipative collapses of primordial pertubations, incorporating star formation, stellar evolution and feedback as well as absorption of starlight by dust, and its re-emission in the infrared. In order to fit the slope of the IRAS number densities, Guiderdoni et al. (1998) introduce a significant population of luminous dust shrouded galaxies, simulating the ultraluminous infrared galaxies (ULIRGs) discovered by IRAS. Still, at $f_\nu(60\,\mu\mathrm{m}) \approx 100$ mJy, their best model (E) is 20% below the number counts found by Hacking et al. (1987).

Another detailed set of galaxy evolution models in the infrared range incorporating the energy emitted by various stellar generations with different abundances, the opacity of the enriched interstellar gas and the flux reradiated by dust has been developed by Franceschini et al. (1994). In order to explain the HH87 60 μm counts Franceschini et al. (1994) favour a model including a population of early type galaxies heavily obscured in the optical by dust.

Optical identification of the HH87 sources has been performed by Ashby et al. (1996) by associating the sources with the closest object on the Palomar Observatory Sky Survey plates within an error circle of 2 arcmin in diameter. From optical spectra Ashby et al. (1996) find a strong concentration of objects at redshifts around 0.088 and all redshifts being lower than 0.26. The redshifts were determined from two or more emission and/or absorption lines, but Ashby et al. (1996) do neither provide information about the identification of the lines nor the line ratios for a detailed classification of the spectra. Only in a few cases there were more than one obvious optical counterpart, but they most often have about the same redshift.

Kawara et al. (1998) have recently presented results from their ISOPHOT survey of a 1.1 deg^2 area in the Lockman Hole region. Their survey was conducted at both 90 μm using the C100 detector and at 175 μm using C200. They find a number density of sources of 33 deg^{-2} at 90 μm down to 150 mJy and 40 deg^{-2} at 175 μm also down to 150 mJy. They find that the number densities at 175 μm are 3–10 times higher than the no-evolution model by Guiderdoni et al. (1998) depending on details in the calibration.

Very recently, the first results of the FIRBACK far infrared survey with the ISOPHOT C200 detector array performed at 175 μm have been published (Puget et al. 1999; Dole et al. 1999). Dole et al. (1999) find that their 175 μm source counts, extracted from a 4 deg^2 area for fluxes down to about 100 mJy, fits well with the E-model by Guiderdoni et al. (1998), while their counts fall in between the Franceschini et al. (1998) models with and without evolution.

Also very recently, the initial results of deep surveys at 850 μm with the first submillimeter detector array, SCUBA, on the James Clerk Maxwell Telescope have been reviewed by Mann (1999). The SCUBA 850 μm source counts down to 1 mJy are in line with the E-model by Guiderdoni et al. (1998) and a few times higher than the model by Franceschini et al. (1998). Due to the limited angular resolution of SCUBA ($\sim$15 arcsec) the optical identification is still somewhat dubious, but many of the sources seem to be associated with optical objects, which have photometric redshifts in the range $1 < z < 3$.

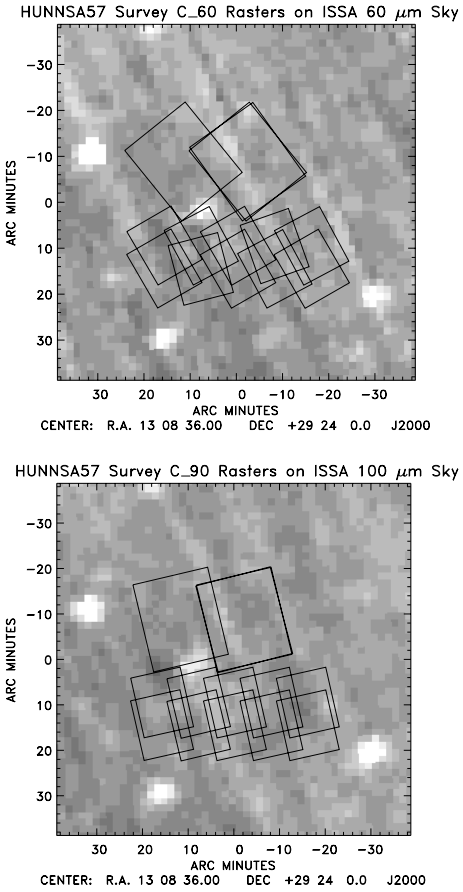

Fig. 1. The areas covered by the raster maps of the HUNNSA57 survey for the two bands are indicated as overlays on ISSA maps. Note the considerable overlap between the individual raster maps

2. The ISOPHOT observations

As part of the Infrared Space Observatory (ISO, Kessler et al. 1996) Central Programme, we have performed a deep ISOPHOT survey of a ~ 0.4 deg^2 area within Selected Area 57 (e.g. Stebbins et al. 1950). We have chosen this area because 1) it is close to the North Galactic Pole and thus has a low far infrared sky background and it is relatively clean with respect to cirrus emission, and 2) because Koo et al. (1986) have identified QSO's in this area down to B = 22.5. With the pre-launch estimate of the performance of the ISOPHOT instrument it was reasonable to expect, that a significant number of these QSO's would be detected in our deep survey.

As an extension to this work we have also included the deep ISOPHOT survey at 90 μm of a 1.1 deg^2 area in the Lockman Hole (Kawara et al. 1998).

We have performed the observations using the ISOPHOT C100 detector array, both at 60 μm and at 90 μm producing three 16×16 arcmin^2 and ten 10×10 arcmin^2 raster maps in each wavelength band. One of the large raster maps is observed twice in each band in order to facilitate consistency checks. In Fig. 1

Table 1. The ISOPHOT observations used in this work identified by their Target Dedicated Time (TDT). The first 11 targets are the HUNNSA57 data, the two next targets are stars observed for calibration purposes and the final eight targets are the observations of the Lockman Hole (Kawara et al. 1998)

	Filter	
Target	C_60	C_90
SA57_1_1	19800825	24300926
SA57_1_1	20401601	24500702
SA57_1_2	19800903	24500804
SA57_2_1	21401405	24601906
SA57_2_2	21800707	24601808
SA57_2_3	21401309	24601710
SA57_2_4	24300711	24500912
SA57_2_5	21401513	24601214
SA57_2_6	21800815	24601516
SA57_2_7	23402817	24601418
SA57_2_8	21401219	24601320
SA57_2_9	21800921	24501022
SA57_2_10	21401023	24601624
α Aql	53400412	–
HR 1654	–	65701316
LH_NW1	–	19400201
LH_NW2	–	19400202
LH_NW3	–	19500103
LH_NW4	–	19500104
LH_E1	–	20800709
LH_E2	–	20800710
LH_E3	–	20900111
LH_E4	–	20900112

the areas covered by the different raster maps for the two bands are indicated as overlays on IRAS Sky Survey Atlas (ISSA) maps (Beichman et al. 1985). The total area covered is 0.40 deg^2 in each band. In order to obtain all data early in the mission, we chose not to constrain the orientation of the rasters. As a consequence there are considerable overlaps between several of the rasters (see Fig. 1). This has given us an additional possibility for investigating the reliability of the obtained data.

The C100 array consists of 3×3 Ge:Ga detectors, each with an angular size on the sky of 43.5×43.5 arcsec^2. Due to gaps between the detector pixels only 93% of the total area of the array is covered. These informations, as well as an extensive explanation of how the C100 detectors are working and details about observing modes including the chopped raster map mode used for the observations described in this work (PHT32) can be found in the ISOPHOT Observer's Manual (Klaas et al. 1994). Further details about the design and performance of the ISOPHOT instrument can be found in Lemke et al. (1993) and (1994) whereas the overall in-flight performance of ISOPHOT is presented by Lemke et al. (1996). We have listed our ISOPHOT observations in Table 1 and the specific instrument setup parameters in Table 2.

As it will be shown below (Sect. 3), the detected sources have a peak intensity of only a few percent of the background level. Since the sky in the survey region is assumed to be very flat, the detectors are illuminated by a nearly constant flux for many hours during these observations. As a consequence transient and memory effects of the detectors are less significant than in other ISO observing modes, where the satellite is moving from the background to bright sources observed for a short time not allowing the detectors to stabilize.

In the following we will present the main instrumental effects which must be considered when reducing ISOPHOT C100 raster map data. It is important to understand, that the ISOPHOT data are measurements of the voltage on the integrating preamplifiers as a function of time. After a specified number of non-destructive read-outs (NRPR-1 in Table 2), the amplifier voltage is reset with a destructive read-out yielding altogether one integration ramp. The change of this voltage with time i.e. the slope of an integration ramp is – ideally – proportional to the incoming flux.

2.1. Non-linearity effects

The Cold Readout Electronics (CRE) of the ISOPHOT instrument exhibit non-linearities i.e. the integration ramps deviate systematically from a linear fit depending on the absolute voltage level of the individual read-outs in the ramp. This effect has an impact on comparisons between integration ramps in different parts of the dynamic range (Acosta-Pulido & Schulz 1996). We have investigated this effect in our data by stacking the measurements according to the read-out number of each ramp and then determining the median value for each read-out number.

Our data indicate that the deviation from linearity is generally less than 1% of the signal. The non-linearity correction implemented in the IDL based ISO**P**HOT **I**nteractive **A**nalysis software package (PIA) (Gabriel et al. 1997) is based on a large number of measurements covering the entire dynamic range of the amplifiers. As illustrated by a typical example in Fig. 2 we find that within the part of the dynamical range occupied by our data no effect is visible.

2.2. Responsivity drift of the individual C100 pixels

As emphasized by Lemke et al. (1996) the responsivity of the C100 pixels can vary in a reproducible way depending on preillumination history and on the accumulated dose of ionizing radiation encountered in orbit. As shown below (Sect. 3), the peak intensity of the point sources detected in this survey is only a few per cent of the sky brightness, so it is crucial to correct the responsivity drift with good accuracy. In Figs. 3 and 4 typical examples of the time ordered data stream for C100 pixels are shown on small and large timescales respectively.

One thing to notice in Fig. 3 is the discrete nature of the read-out voltages caused by the finite resolution of the read-out electronics. Here the dynamic range of 2.5 V are digitized using twelve bits or 4096 values resulting in voltage steps dU = 2.5 V / 4096 = 0.61 mV. In the data reduction this discretisation is however of no major concern since the signal is obtained by fitting a first order polynomial to each integration ramp. In Fig. 3

Table 2. Main parameters for the observations: Filter (see Klaas et al. 1994), Mode - observing mode, AOT - Astronomical Observing Template (see Klaas et al. 1994), nY (number of raster points along the spacecraft Y axis), nZ (number of raster points along the spacecraft Z axis), dY (step size along the spacecraft Y axis), dZ (step size along the spacecraft Z axis), NRPR (number of read-outs per integration ramp), $t_{read-out}$ (time per read-out interval), NRCP (number of integration ramps per chopper plateau), NCHP (number of chopper steps per pointing), CHST (chopper step size) and NSWP (integer number of chopper sweeps per pointing). The first four measurement types are the large and small science rasters for both bands, the next two types are the science rasters for the calibration measurements, then the measurement type for the Lockman Hole data and finally the parameters for the FCS measurements are listed

Filter	Mode	AOT	nY	nZ	dY [″]	dZ [″]	NRPR	$t_{read-out}$ [ms]	NRCP	NCHP	CHST [″]	NSWP
C_60	Chopping	PHT32	11	14	92	69	16	31.25	4	13	15	3
C_60	Chopping	PHT32	7	9	92	69	16	31.25	4	13	15	4
C_90	Chopping	PHT32	11	14	92	69	8	31.25	4	13	15	2
C_90	Chopping	PHT32	7	9	92	69	8	31.25	4	13	15	3
C_60	Chopping	PHT32	2	15	60	15	8	31.25	4	13	15	3
C_90	Chopping	PHT32	3	3	60	46	8	31.25	4	13	15	3
C_90	Staring	PHT22	18	18	69	69	64	31.25	–	–	–	–
FCS	Staring	PHT32	–	–	–	–	64	31.25	–	–	–	–

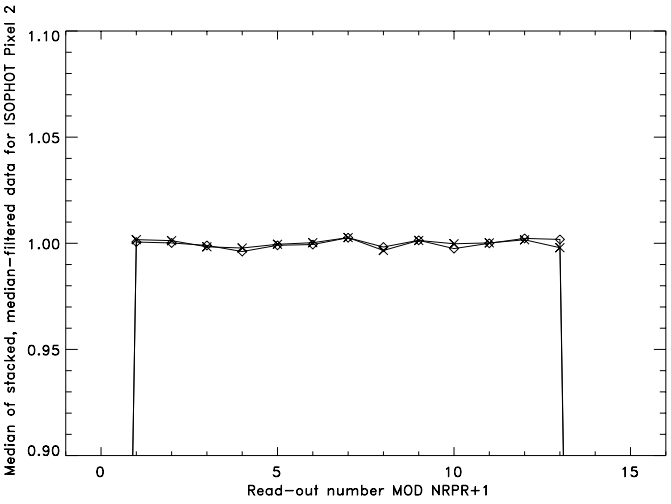

Fig. 2. Illustration of the very low level of non-linearity of the read-out electronics for pixel 2 in one of our a C_60 raster maps (NRPR $= 16$). Here the first and the two last read-outs per ramp have been discarded as is also the case in our data reduction. Crosses indicate data with PIA non-linearity correction applied and diamonds without correction. Before stacking the read-outs the data stream has been divided by a median filtered version of the data in order to remove drift (see Sect. 2.2) resulting in data values around 1

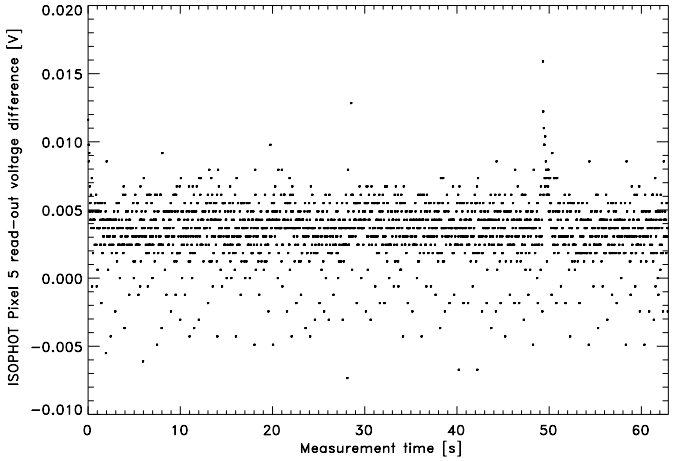

Fig. 3. An example of the temporal behaviour of one of the pixels in the C100 array. The read-out voltage difference between consecutive read-outs as a function of time exhibits no obvious drift. Note the discrete nature of the read-out voltages caused by the finite digital resolution of the read-out electronics. Note also a glitch event (see Sect. 2.3) at a measurement time of ~ 50 s

one further notices a glitch event at a measurement time of 50 s. These events are discussed further in Sect. 2.3.

It can be seen that variations exist mainly on long timescales which are comparable with the duration of the entire measurement (Fig. 4a). On much shorter timescales, as shown in Fig. 3, no obvious drift is detectable. As it can be seen from Fig. 4a there is also an initial transient period where the detector stabilizes. We have performed a detailed investigation of this behaviour by inspecting the measurement timeline for each pixel in each raster represented by the median signal per raster point as a function of time. In most cases a characteristic behaviour emerges as illustrated in Fig. 4a. The signal first exhibits a transient with a steep rise, a sharp break and then a more slowly increasing baseline level. Pixels 1 and 5 demonstrate this behaviour all the time whereas other pixels – especially pixel 6 – are somewhat more unpredictable. The frequency of rasters with a well-defined break and the related mean time for the break are listed for each pixel in Table 3. Note that the break time is defined as the time corresponding to the point where the two fitted first order polynomials intersect (see Fig. 4a) and the frequency is given in percent of the total number of rasters in each band (i.e. 13). The distributions of break times and slopes of the first order polynomial fitted to the initial transients are shown for pixel 5 in Fig. 5.

The initial transient period lasts 642 ± 138 s for the C_60 data and 312 ± 52 s for the C_90 data. This factor of two may

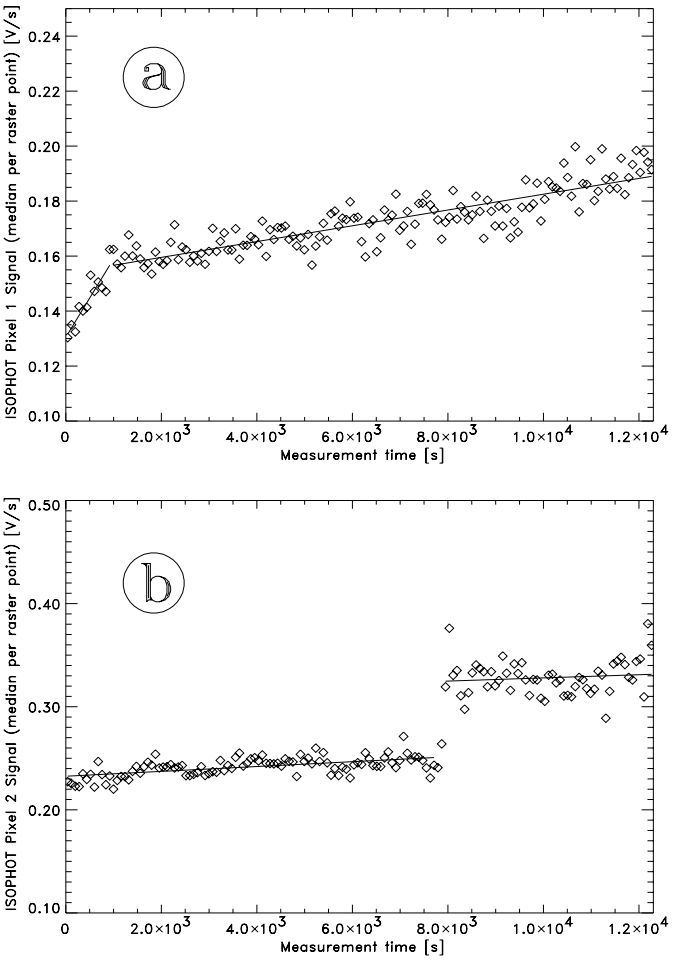

Fig. 4a and b. Two examples of the temporal behaviour of the detector signal (median value per raster point) of some of the pixels in the C100 array. In **a** a typical behaviour with initial, steeply rising transient, break and slow rise is shown whereas **b** is an example of a somewhat more bizarre behaviour with an abrupt jump in the signal level and increased scatter around the linear fit after the jump

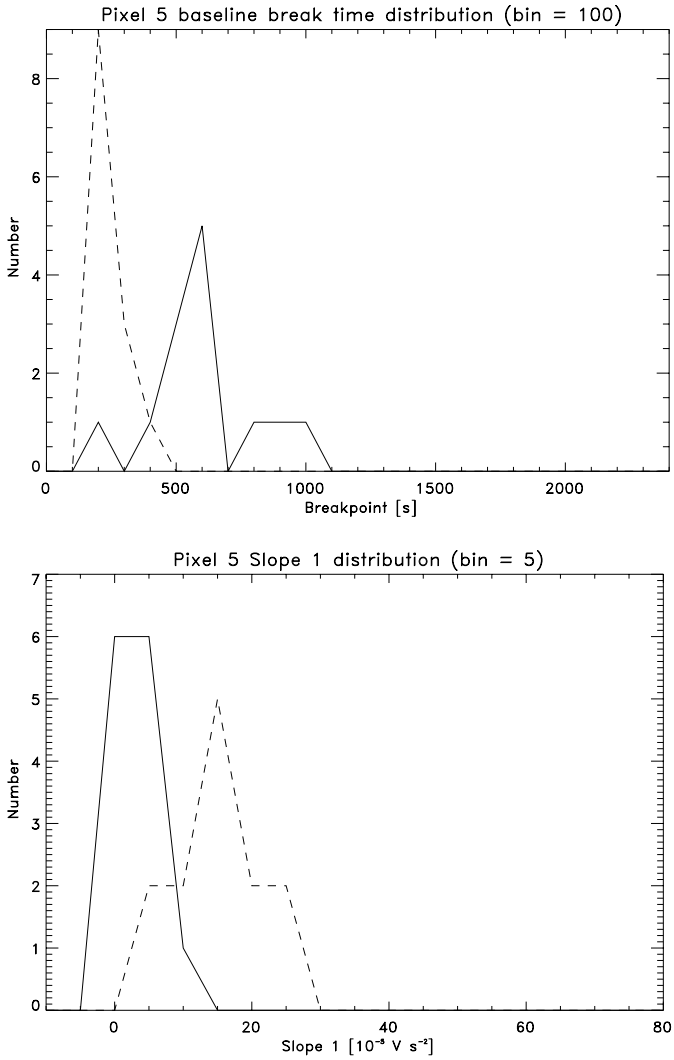

Fig. 5. Distributions of baseline break times and slopes of the 1st order polynomium fit to the initial transient. Solid lines represent C_60 data and dashed lines C_90 data. It is obvious that there is a systematic difference between data obtained in the two bands. This behaviour may be related to the fact that the C_60 data have twice as many read-outs per integration ramp as the C_90 data

be related to the fact that the C_60 data have twice as many read-outs per integration ramp as the C_90 data.

Distortions of the data like the abrupt jump seen in Fig. 4b are not very frequent. Out of the 26 raster maps such behaviour is seen four times for pixels 4 and 9, two times for pixels 2, 5, 7, 8, once for pixel 3 and never for pixels 1 and 6.

The average increase in signal from the start of the measurement until the breakpoint is $\sim 15\%$ of the initial level for the C_60 data and $\sim 20\%$ for the C_90 data. For the remaining part of the measurement the signal increase is $\sim 15\%$ of the initial level for the C_60 data and $\sim 20\%$ for the C_90 data.

With the responsivity variations seen in Fig. 3 and 4, it is clear, that a simple box filtering of the data will not be an appropriate technique. We have instead employed a median filtering technique in our data reduction to minimize the influence of large deviations. This method – described below in Sect. 3 – has demonstrated a good ability to remove effects like the ones

Table 3. Percentage of rasters with *baseline-break* and mean time for break. The last column gives the mean scatter around the long linear part (see Fig. 4a) for all 26 raster maps. This scatter is in percent of the start-level for the linear part

	C_60 data		C_90 data		
Pixel	%	t_{break} [s]	%	t_{break} [s]	Scatter [%]
1	100	704	100	352	3.3
2	54	800	54	358	3.3
3	69	647	92	365	3.4
4	77	402	92	248	3.0
5	100	628	100	284	3.8
6	23	820	8	322	6.3
7	77	662	92	260	2.9
8	62	459	100	251	2.8
9	100	655	92	369	4.0

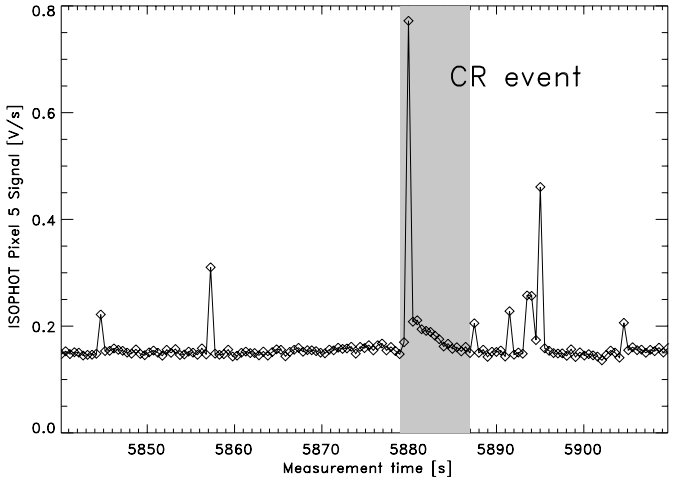

Fig. 6. Example of the effect of a cosmic ray induced glitch in the data stream (signal-level). The grayshaded region represents a subjective estimate of which signals are affected by the event, but a consistent method for such a discrimination has not yet been established

shown in Figs. 4a and 4b allowing these data to be included in the final mapping.

2.3. Glitches affecting the data stream

Also glitches induced by cosmic ray events have to be removed from the data. In Fig. 6 we show a typical example from the time ordered data stream of the effect of such a glitch.

We have performed a detailed analysis of glitches in our data in order to establish important quantities such as the overall glitch rate and the glitch rate per pixel. The data have been analysed per raster point by determining mean and σ for a gaussian fitted to the distribution of voltage differences of consecutive read-outs per pointing. All voltage differences 3σ above – and only above – the mean are regarded as glitches (see Linden-Vørnle 1998 for details) yielding the glitch rates listed in Table 4. Here it can be seen that each pixel is affected about once every 2 s meaning that almost every chopper-plateau in the C_60 data and every second in the C_90 data and the standard star data is affected at least once by a glitch. It is furthermore worth noticing that there are significant systematic differences between the glitch rates of the individual pixels – an effect most likely related to spontaneous spiking.

It is worth noticing that pixel 8 has a significantly lower glitch rate. The reason for this is probably that this pixel generally has a higher scatter in the voltage differences of consecutive read-outs. This results in a higher threshold for glitch detection and therefore a lower rate for the weakest – and most frequent – glitches. The lower rate for pixel 8 is therefore not an indication of this pixel being less noisy – rather the opposite situation is the case.

The behaviour of individual pixels just after a glitch is very unpredictable. Although many efforts have been made, we have not yet succeeded in establishing any usefull correlation e.g. between the read-out voltage amplitude of the initial jump and the time evolution of the transient following immediately after the glitch. Even after a strong glitch the read-outs after the event sometimes seem well-behaved compared to the read-outs just before the glitch, while in other cases a glitch of similar strength, affects many subsequent read-outs.

As a consequence, no attempts have been made to correct the data affected by glitches and instead we have tried to optimize our reduction in order to assure a minimal influence from the glitches on the final maps.

Table 4. Glitch rates for the HUNNSA57 data. First the total rate and the rate per pixel assuming that each pixel is hit the same number of times (i.e. total rate $\times$ 1/9) is given. Then the rates per filter are given and finally the rates for the individual C100 pixels are listed. These last values represent the mean and scatter over all raster maps i.e. both C_60 and C_90 data

All data:	$6.43\,\mathrm{s}^{-1}$
All data per pixel:	$0.71\,\mathrm{s}^{-1}$
C_60 filter:	$6.56\,\mathrm{s}^{-1}$
C_90 filter:	$6.06\,\mathrm{s}^{-1}$

Pixel	rate [s^{-1}]
1	0.66 ± 0.11
2	1.49 ± 0.19
3	0.64 ± 0.12
4	0.95 ± 0.21
5	0.69 ± 0.10
6	0.59 ± 0.08
7	0.60 ± 0.10
8	0.23 ± 0.02
9	0.40 ± 0.08

2.4. Chopper dependent signal offset

We have also used our data to determine the signal offset of the different pixels at different chopper positions. This effect is caused by slightly unbalanced beams in both chopper end positions. Again we are exploiting the fact that our observations are presumably performed under very stable conditions, that there are only a few point sources per raster, and they are all faint relative to the sky background. After the removal of the drift we stack the measurements for each raster and pixel according to the chopper position and then determine the median for each chopper position. In Fig. 7 a typical example can be seen in comparison with the standard PIA signal offset correction factors. In general the effect of the chopper dependent signal offset is in the order of 1% or lower and has therefore not been included in our data reduction scheme.

3. Data reduction

Following the presentation of the various instrumental effects in the previous section we here briefly outline our data reduction scheme. The backbone of the reduction is PIA version 7.3.1(e) where the processing is performed on various data-levels, namely: Edited Raw Data (ERD), Signal Raw Data (SRD), Signal per Chopper Plateau data (SCP) and finally Astronomical Analysis Processing (AAP). We have used batch processing from ERD- to AAP-level using the processing steps listed in Table 5. Since our data do not seem to be strongly af-

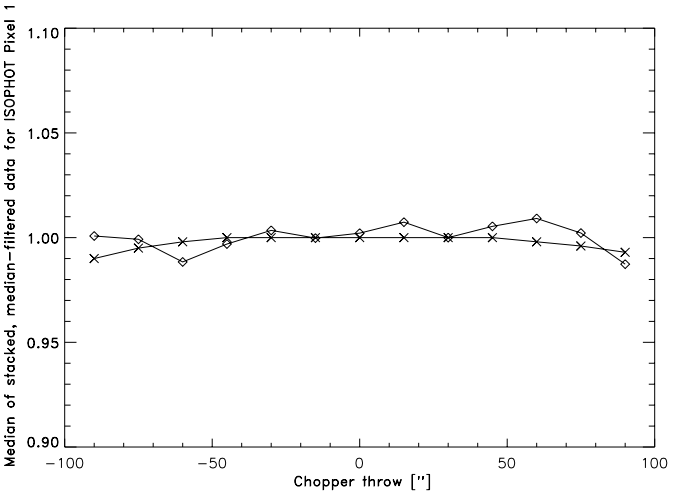

Fig. 7. Example of chopper dependent signal offset for pixel 1 in the C100 array. Diamonds indicate the offset found in our data whereas crosses represent the standard PIA signal offset correction values

Table 5. Processing steps used in the PIA batch reduction from ERD- to AAP-level

Level	Processing step
ERD	Two-threshold deglitching
ERD→SRD	1. order pol. fit to ramps
SRD	Reset interval correction
SRD	Signal deglitching
SRD	Orbital dependent dark current subtraction
SRD→SCP	No drift handling
SCP→AAP	Actual responsivity flux-calibration using only FCS1 in the FCS-measurement following the science raster

fected by non-linearities (see Sect. 2.1) this correction is omitted at the ERD-level. Similarly we have not performed signal offset correction on the SCP-level. We have furthermore reduced the data from SRD- to SCP-level not using the PIA drift handling option since we have employed our own non-PIA IDL routine to remove the baseline drift. This routine removes the drift in two steps. First the time ordered AAP-data are filtered using a narrow median window in order to remove remaining data affected by glitches. After this removal of high frequency noise we apply a much broader median filter and then divide the data with the filtered version in order to remove the large scale drift thus flatfielding the data. The map is then rescaled to sky brightness using the mean value of the sky brightness from each of the nine pixels. We have carefully optimized the width of the drift filter in order to secure that the statistical properties of the data are generally preserved after filtering.

After drift handling is done for the AAP-level data, PIA is used to produce maps. We have chosen to exclude data from pixels 6 and 8 due to the fact that pixel 6 generaly exhibits very unstable performance and pixel 8 as a rule is about a factor of two more noisy than the other pixels. For the mapping we use $15 \times 23\ \mathrm{arcsec}^2$ pixels which areawise is about 1/6 of a detector pixel. This pixel size is chosen since it naturally arises from the combination of 15 arcsec chopper movement steps and the raster step size along the spacecraft Z axis (2/3 oversampling).

Table 6. Parameters used in the source detection using SExtractor version 1.2

Parameter	Value
DETECT_MINAREA	9
DETECT_TRESH	2.25
BACK_SIZE	64

3.1. Source extraction

In order to detect individual sources we have employed the SExtractor software, verion 1.2 (Bertin & Arnouts 1996). Each raster map has been analysed with the parameters given in Table 6. These parameters have been established by investigating the parameter space for the source extraction for the repeated large rasters (SA57_1_1 in Table 1) which have almost 100% area overlap. The requirement for the parameters is that they should yield consistent results while minimizing the detection area and σ-level constraints i.e. going as faint as possible.

For a source detection to be classified as reliable we set the requirement that in areas where the raster maps are overlapping a detection must be confirmed in the overlapping raster map(s) observed in the same band within an error-ellipse with radius 10 arcsec. Non-confirmed sources in overlapping areas are presently considered to be dubious detections. In areas without any overlap we must rely on the robustness of the extraction parameters chosen. Due to the increasing noise at the edges of the maps detections closer than 45 arcsec to the edges are however rejected.

We have coadded the raster maps (see Fig. 8) resulting in a decrease in noise in the overlapping areas. Running SExtractor on these coadded maps results in more detections but only in high-noise i.e. non-overlapping regions. This effect is due to the overall reduction of the scatter in the background resulting in a lower detection threshold.

With the chosen SExtractor parameters listed in Table 6 the detected sources have a formal signal to noise ratio, SNR ≥ 6.75.

3.2. Flux calibration

As indicated in Table 5 the flux calibration is done using the internal Fine Calibration Sources (FCS). We have analysed the FCS measurements performed both before and after the science raster using PIA and the settings listed in Table 5 (up to the SCP-level) and we find that the scatter in the derived sky brighness is significantly smaller for the FCS measurements performed after the science raster. As a result only the FCS measurement following the science raster has been used in our batch-processing to derive actual responsivities.

In order to correct the source signal found within the detection area to obtain the total flux, we have simulated the PHT32

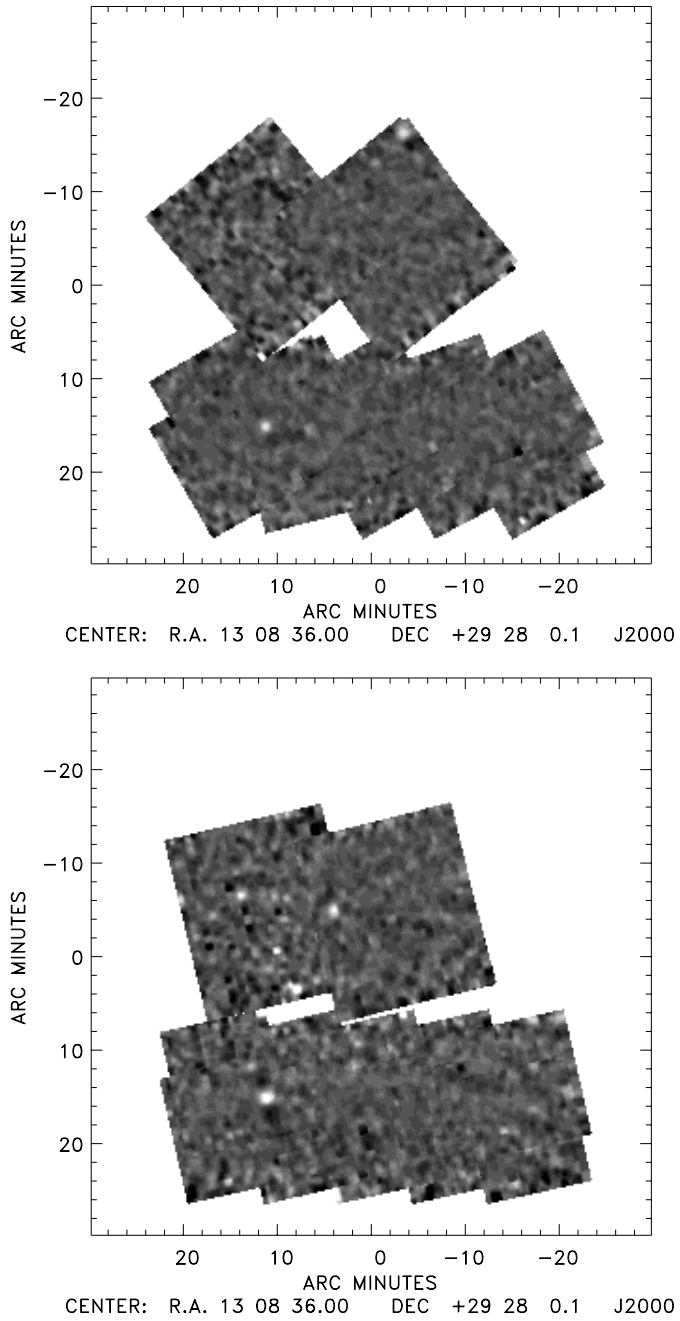

Fig. 8. Coadded maps at 60 μm (top) and 90 μm (bottom)

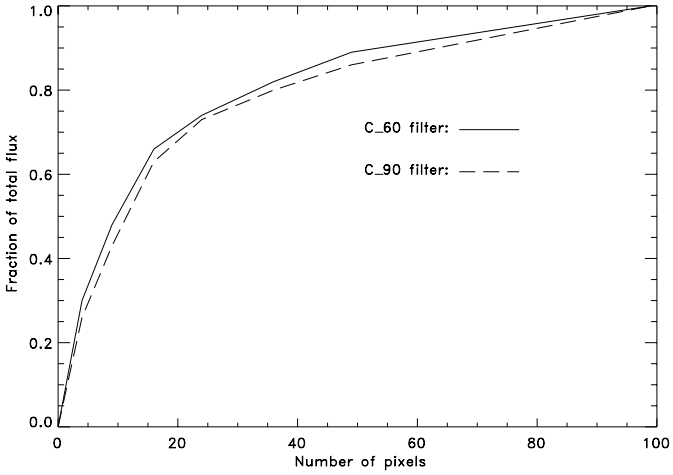

Fig. 9. Relation between detection area in terms of 15×23 arcsec^2 sky pixels and fraction of total flux for both filters

Table 7. Comparison of the COBE DIRBE and the ISOPHOT (PHT) sky brightness [MJy sr^{-1}]. D/P is the DIRBE/ISOPHOT ratio

Sky at target	DIRBE	PHT	D/P
α Aql, C_60	12.85 $\pm$0.34	14.36 $\pm$1.32	0.90
HR 1654, C_90	4.79 $\pm$0.10	6.52 $\pm$0.36	0.74
HUNNSA57, C_60	9.91 $\pm$0.10	8.78 $\pm$0.64	1.12
HUNNSA57, C_90	4.72 $\pm$0.04	6.15 $\pm$0.20	0.77
Lockman Hole, C_90	3.93 $\pm$0.08	5.22 $\pm$0.20	0.75

mapping procedure assuming a linear response and then used it on the point spread functions for C100 with C_60 and C_90 filters, taken from the calibration file PC1FOOTP.FITS. In Fig. 9 the resulting relations between the size of the detection area (number of 15×23 arcsec^2 pixels) and the fraction of the total flux for both C_60 and C_90 is shown.

In Table 7 the resulting sky brightnesses are listed and compared to the COBE DIRBE (Hauser et al. 1997) annual average values. We have verified that the comparison between ISOPHOT and DIRBE annual average values is viable by checking the DIRBE/ISOPHOT ratio for DIRBE weekly maps, which include the variable contribution from the Zodiacal Light. The ratios thus obtained are very similar to those listed in Table 7 with a scatter of only 7% for C_60 and 3% for C_90. In total it can be seen that the ISOPHOT and DIRBE surface brightness values are in agreement within about 10% for C_60 and 25% for C_90.

In order to calibrate the source signals found by SExtractor to an absolute flux scale we have used observations of α Aql (C_60) and HR 1654 (C_90), observed with nearly the same instrument parameters as the HUNNSA57 raster maps (see Table 2). Both stars have been detected by IRAS with a 60 μm flux for α Aql of 1250 mJy $\pm$11% (IRAS PSC; flux quality = 3) and a 100 μm flux for HR 1654 of 579 mJy $\pm$24% (IRAS FCS; flux quality = 2). More recently a model flux for α Aql has however been established as part of the ISO calibration ground-based preparatory programme (GBPP, Jourdain de Muizon & Habing 1992 and van der Bliek et al. 1996) and similarly a C_90 model flux for HR 1654 has been found by fitting the shape of an appropriate red giant branch spectral energy distribution (SED) model to near-IR and mid-IR observations obtained for this star, thus extending the SED out to 300 μm (Cohen et al. 1996, Cohen private communication). This way the following model fluxes have been obtained: 902.9 mJy and 712.6 mJy, for α Aql (C_60) and HR 1654 (C_90) respectively. We have chosen to adopt these model fluxes for use in our calibration.

In order to obtain these model fluxes from our observed source signals of the standard stars, using the correction for source signal lying outside the detection area given in Fig. 9,

Table 8. Astrometry and photometry (in mJy) for the reliably detected sources in the HUNNSA57 and Lockman Hole data. For the HUNNSA57 data $n(60\,\mu\mathrm{m})$ and $n(90\,\mu\mathrm{m})$ gives the number of detections in independent rasters over number of possible detections (i.e. 2/2 means two detections out of two possible). For sources with two or more detections in the same band position and flux is given as the mean of the values from the individual detections. For these multiple detections the scatter, sc, of the individual values is given in arcsec for the positions and mJy for the fluxes. For sources only seen in one band upper limit for the flux in the other band based on the detection criteria listed in Table 6 is given. Note that no 90 μm flux upper limit is given for HUNNSA57_6 since this source lies outside the area covered in this band. Since there is no redundancy in the Lockman Hole data only SNR values for each source is given ($\sigma = 17$ mJy). One of the Lockman Hole sources has been detected by IRAS. For this source the IRAS flux is given

Source name	$n(60\,\mu\mathrm{m})$	$n(90\,\mu\mathrm{m})$	α(2000)	sc_α	δ(2000)	sc_δ	$f_\nu(60\,\mu\mathrm{m})$	$sc_{f_\nu(60\,\mu\mathrm{m})}$	$f_\nu(90\,\mu\mathrm{m})$	$sc_{f_\nu(90\,\mu\mathrm{m})}$
HUNNSA57_1	3/3	3/3	13 09 28	$2''$	29 12 47	$5''$	243	61	173	13
HUNNSA57_2	0/2	2/2	13 08 55	$1''$	29 32 54	$4''$	< 90		178	55
HUNNSA57_3	0/1	1/1	13 09 40		29 34 34		< 110		98	
HUNNSA57_4	0/1	1/1	13 08 44		29 18 50		< 90		68	
HUNNSA57_5	0/1	1/1	13 08 45		29 16 02		< 90		82	
HUNNSA57_6	2/2	0/0	13 08 20	$7''$	29 44 26	$8''$	236	26	–	
HUNNSA57_7	0/1	1/1	13 09 14		29 24 31		< 110		162	

Source name	α(2000)	δ(2000)	$f_\nu(90\,\mu\mathrm{m})$	SNR	IRAS $f_\nu(100\,\mu\mathrm{m})$
Lockman NW1_1	10 32 36.9	58 08 53.7	331	20	
Lockman NW1_2	10 32 04.4	58 08 05.1	203	12	
Lockman NW2_1	10 36 04.6	57 47 57.2	265	16	
Lockman E1_1	10 50 51.7	57 35 17.0	197	12	
Lockman E1_2	10 49 48.1	57 34 58.1	165	10	
Lockman E4_1	10 53 49.8	57 07 20.5	747	45	1218
Lockman E4_2	10 53 02.7	57 05 51.1	177	15	
Lockman E4_3	10 52 53.0	57 08 16.3	203	12	

we find a factor of 2.51 for C_60 and 1.41 for C_90 has to be applied.

Based on the detection criteria given in Table 6 and the empirical calibration factors established above our source detection limit with a formal SNR = 6.75 is 90 mJy for C_60 and 50 mJy for C_90.

It is well known that the instant response to a change in flux for photoconductors such as the ISOPHOT C100 detector usually is only a fraction of the stabilized response. In our observations the detector is observing the sky background for a long time allowing the detector to reach the stabilized response. When the detector moves onto a weak point source and then returns to the sky again there has not been enough on-source time to reach the stabilized response for the source. It is therefore not unexpected that point source calibration factors as those established above would emerge as part of the calibration.

It is however not easily possible to test these empirically established point source calibration factors of 2.51 for 60 μm and 1.41 for 90 μm. In order to do so one could imagine simulations where sources of known flux are introduced in the data and then extracted using the same procedure as for the real sources. This could in principle verify the validity of the correction factors and yield a completeness correction as a function of flux. In order to perform a realistic simlulation like that, systematic effects at all levels of the data reduction would have to be understood. Since the noise properties of the resulting sky maps are dominated by highly correlated effects emanating from glitch residuals and since no detailed understanding of glitch behaviour is currently available, we believe that such simlulations are not feasible at the present time.

In Table 8 the reliably detected HUNNSA57 sources with astrometry and photometry are listed. For each source $n(60\,\mu\mathrm{m})$ and $n(90\,\mu\mathrm{m})$ indicate the number of detections in independent rasters over number of possible detections in these rasters (i.e. 2/2 means two detections out of two possible). For sources with more than one detection the position and fluxes listed is the mean of the values from individual detections. For these multiple detections the scatter of the individual detections is given as sc_α and sc_δ for the position (in arcsec) and $sc_{f_\nu(60\,\mu\mathrm{m})}$ and $sc_{f_\nu(90\,\mu\mathrm{m})}$ for the fluxes (in mJy). For sources only detected in one band upper limits are given for the other band. These limits have been calculated using the noise estimate from SExtractor for the relevant map and the criteria listed in Table 6.

Two of the sources, HUNNSA57_1 and HUNNSA57_6, are IRAS Faint Sources with good 60 μm fluxes (IRAS quality flag 3). The IRAS fluxes are compared with our values in Table 9 and it can be seen that the agreement is good within $\sim 10\%$.

Based on the results listed in Tables 7 and 9 we are confident that we have established a reliable calibration which yields a sky brightness in agreement with COBE DIRBE results and point source fluxes consistent with IRAS FSC at least for 60 μm. IRAS F13059+3000 also has a good 100 μm flux but unfortunately this source lies just outside our C_90 raster maps prohibiting an independent check of our 90 μm calibration. Based on the agreement with DIRBE and the scatter of source fluxes from in-

dependent maps (see Table 8) we estimate that our photometric uncertainty for point sources is about 25%.

3.3. Analysis of the ISOPHOT Lockman Hole data

As mentioned in Sect. 1 we have included the ISOPHOT observations of a 1.1 deg^2 blank field in the Lockman Hole area (Kawara et al. 1998) in this work. We have reduced the C_90 data using the same batch processing steps as outlined in Table 5 and also removed drift at the AAP-level using median filtering. We have adopted a similar median filter width as Kawara et al. (1998) namely the number of pointings along a raster leg $\times$ 1.5. Source extraction is also performed using SExtractor with parameters similar to those listed in Table 6. Only the parameter for minimum detection area, DETECT_MINAREA, was trimmed to 11 instead of 9. Since there is no significant overlap between the eight rasters we have not been able to optimize the extraction parameters in the same way as for the HUNNSA57 data but rely instead on the robustness of the method.

Regarding calibration we find that the sky brightness in the C_90 data resulting from the ISOPHOT FCS calibration yields a sky background which is about 30% brighter than the DIRBE annual average value (see Table 7). This is in fairly good agreement with our findings for the HUNNSA57 data. Regarding point sources, we have simulated the PHT22 mapping mode again assuming a linear response in order to establish the relation between the observed flux and the detection area (number of pixels – here 23×23 arcsec^2). After using this relation to correct the source signals found by SExtractor to obtain the total flux we have applied our empirical C_90 calibration factor of 1.41 obtained from the standard star observations (see Sect. 3.2). Astrometry and photometry for the detected sources is given in the second part of Table 8. Since there is no redundancy in the Lockman Hole data in the sense of positions and fluxes from independent raster maps we only list SNR values for the detected sources. As indicated in Table 8, the source Lockman E4_1 has also been detected by IRAS (F10507+5723) with an IRAS 100 μm flux of 1218 mJy. With the calibration established in this work this flux is underestimated by 63%. Kawara et al. (1998) use this IRAS source to calibrate their point source fluxes and therefore fluxes and flux limits presented by Kawara et al. (1998) have to be corrected by a factor of $(1.0+0.63)^{-1} = 0.61$ in order to allow comparison with our results.

4. Discussion

As it can be seen from the coadded HUNNSA57 maps in Fig. 8 point sources are sitting on top of a largely structureless background. This is expected since our median filtering technique suppresses extended structure in the background. The brightness variations in the individual C_90 maps have an rms of about 0.5 MJy sr^{-1} equivalent to 6 mJy per 15×23 arcsec^2 pixel. This compares well to the results obtained by Herbstmeier et al. (1998) where observations of a smooth area on the sky, M03, selected for studies of structure in the zodiacal light yields fluctuations at the 6 mJy level per 46×46 arcsec^2 pixel. Both our value and the value found by Herbstmeier et al. (1998) is considerably higher than the expected one sigma confusion noise for infrared cirrus of $\sigma_{cirrus}(90\mu\mathrm{m}) \sim 0.14$ mJy for a 23×23 arcsec^2 pixel presented by Kawara et al. (1998).

Table 9. Flux comparison for IRAS faint sources in the HUNNSA57 sample. The flux is given in mJy

Source name	HUNNSA57_1	HUNNSA57_6
IRAS name	F13071+2928	F13059+3000
PHT $f_\nu(60\,\mu\mathrm{m})$	243 $\pm$61	236 $\pm$26
IRAS $f_\nu(60\,\mu\mathrm{m})$	266 $\pm$42	269 $\pm$43
PHT/IRAS	0.91	0.88

As it can be seen from Table 8 we have in our HUNNSA57 survey detected seven sources at 90 μm brighter than 68 mJy and two sources at 60 μm brighter than 236 mJy. Only one of the sources, HUNNSA57_1, is detected in both bands yielding a flux ratio, $\frac{f_\nu(90\,\mu\mathrm{m})}{f_\nu(60\,\mu\mathrm{m})} = 0.7$. For the HH87 60 μm sources, which also have a moderate-quality 100 μm flux, the mean flux ratio $\frac{f_\nu(100\,\mu\mathrm{m})}{f_\nu(60\,\mu\mathrm{m})}$ is 3.1 whereas only 8% of the sources have a flux ratio ~ 1. One of these sources is the nearby galaxy NGC 6552, which is identified as a Seyfert 2 galaxy (see e.g. Bassani et al. 1999). For a low redshift galaxy, assuming a grain emissivity index of 1.5, a flux ratio $\frac{f_\nu(90\,\mu\mathrm{m})}{f_\nu(60\,\mu\mathrm{m})} = 0.7$ actually corresponds to a dust temperature of ~ 65 K whereas a ratio of 3.1 corresponds to a temperature of about 25 K. This seems to indicate that our source, HUNNSA57_1, might have a dust component with a temperature of about 65 K, maybe harbouring an active galactic nucleus. The detailed characteristics of this and the other sources will be discussed further in paper II dealing with the individual sources supplemented by optical images and spectra.

For the observations of the Lockman Hole the number of reliably detected sources amounts to eight down to 165 mJy which is somewhat more conservative than the result of 36 sources down to 90 mJy reported by Kawara et al. (1998). Based on our experience with the redundant HUNNSA57 data we are however – at this stage – not confident about detections below our limit of 165 mJy. Furthermore Kawara et al. (1998) do not in detail describe their criteria for finding sources. Note that the flux limit reported Kawara et al. (1998) is 150 mJy which here has been corrected by a factor of 0.61 in order to match our calibration as described in Sect. 3.3.

As mentioned in Sect. 2 the total area is 0.40 deg^2 in both bands for the HUNNSA57 survey. This also takes into account the area lost by rejecting sources at the edges. For the Lockman Hole data the area is 1.1 deg^2. The cumulative number counts at 90 μm down to 150 mJy are 14.8 per deg^2 and at 60 μm 5 per deg^2 down to 90 mJy. Compared to the number counts coming from the Guiderdoni et al. (1998) no-evolution model i.e. no evolution of neither source density nor luminosity and a cosmology with $h = 0.5$ and $\Omega_0 = 1$ our number counts indicate a number density which is higher by a factor of 1.8 ± 0.6 for 90 μm but are inconclusive for 60 μm.

In Fig. 10 the number density of 60 μm sources from our HUNNSA57 survey is plotted together with previously pub-

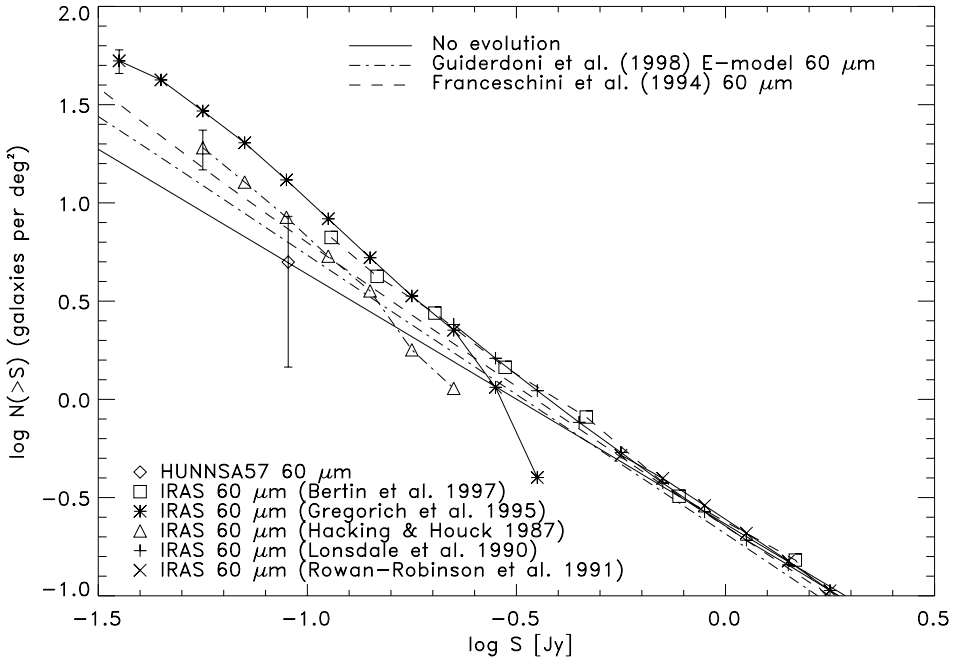

Fig. 10. Cumulative 60 μm number counts for HUNNSA57 along with previously published source counts and models. Our data are plotted with with error bars representing Poissonian uncertainties whereas the previously published source counts are plotted without error-bars

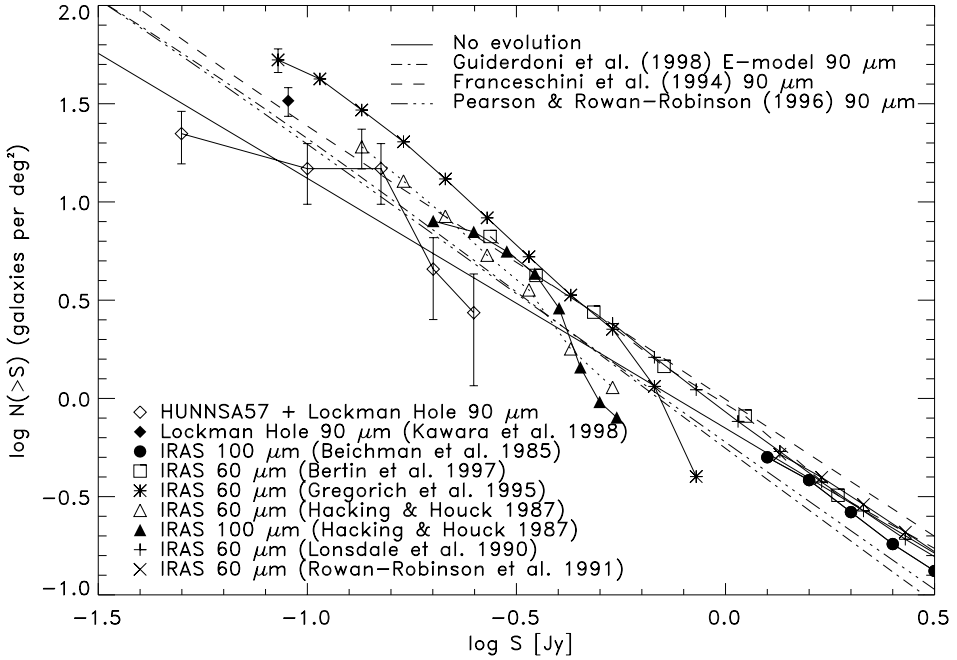

Fig. 11. Cumulative 90 μm number counts for HUNNSA57 + Lockman Hole data along with previously published counts and models. Except for the IRAS 100 μm data from Beichman et al. (1985) and HH87 the previously published counts are actually the 60 μm counts presented in Fig. 10 with the flux scale multiplied by a factor of 2.4. This factor has been established as the flux factor between the IRAS 60 μm and 100 μm point source counts at $|b| > 50^\circ$ and we have verified that this scaling is valid at least for low redshift galaxies ($z \leq 0.5$) with dust temperatures in the range 30–40 K and an emissivity indices ranging from 1 to 2. As in Fig. 10 our data are plotted with error bars representing Poissonian uncertainties whereas the previously published source counts are plotted without error bars except for the Kawara et al. (1998) data and the faintest bin of the Hacking & Houck (1987) and Gregorich et al. (1995) data. Note that the flux limit of the Kawara et al. (1998) data has been corrected as discussed in Sect. 4 in order to match up with our calibration

lished counts from Bertin et al. (1997), Gregorich et al. (1995), Hacking & Houck (1987), Lonsdale et al. (1990) and Rowan-Robinson et al. (1991). Due to the large number of data points the previously published data are plotted without error bars. The evolution model from Franceschini et al. (1994) which includes an early population of dust shrouded galaxies and the Guiderdoni et al. (1998) E-model which introduces a rapidly increasing fraction of ULIRGs with redshift are included. Also

the no-evolution model from Guiderdoni et al. (1998) mentioned above is included.

In Fig. 11 the 90 μm number densities found from the combined HUNNSA57 and Lockman Hole surveys are plotted in a similar way also including evolutionary models from the references listed above plus the model from Pearson & Rowan-Robinson (1996) which includes a strongly evolving population of dusty starburst galaxies which absorb 90–95% of the optical light and re-emit it at infrared wavelengths.

In order to compare with source count data we have done three things. First we have included 100 μm counts from the IRAS PSC (Beichman et al. 1985) which are the only published 100 μm number counts from IRAS and secondly we have included source counts of the HH87 sources with moderate-quality 100 μm flux excluding of course NGC 6543 and another source noted by HH87 to be cirrus. It is important to note that the 100 μm sources from HH87 do not represent an independent sample but are instead 100 μm fluxes determined at the positions of the detected 60 μm sources. Finally we have multiplied the flux scale of the 60 μm counts shown in Fig. 10 by a factor of 2.4. This factor has been established as the flux factor between the IRAS 100 μm and 60 μm Point Source counts at $|b| > 50^\circ$ (Beichman et al. 1985) at equal number densities. It has been confirmed to us that such a scaling is viable since the area coverage for the 60 μm and 100 μm number counts is identical (T. Chester, IPAC, private communication). The IRAS 100 μm and ISOPHOT C_90 filter exhibit fairly similar spectral response and we have verified that the scaling factor 2.4 is valid to within a few percent at least for low redshift galaxies ($z \leq 0.5$) with dust temperatures in the range 30–40 K and grain emissivity indices ranging from 1 to 2. This also implies that the IRAS 100 μm number counts can be directly compared with the ISOPHOT 90 μm data. As in Fig. 10 the previously published source count data plotted in Fig. 11 are shown without error bars except for the faintest bin of the Hacking & Houck (1987) and Gregorich et al. (1995) data.

From Fig. 10 it can be seen that the sparseness of our data do not allow us to make any strong statements about the 60 μm population. With our 60 μm detection limit of 90 mJy at the formal SNR of 6.75 it is noteworthy that we do not find any sources in the flux range from 236 mJy to 90 mJy. This situation is probably a result of the small survey area by chance missing out fainter sources.

For the 90 μm data in Fig. 11 the combined HUNNSA57 and Lockman Hole number densities are in line with evolutionary models by Guiderdoni et al. (1998), Pearson & Rowan-Robinson (1996) and Franceschini et al. (1994) without being able to discriminate between them. Also the no-evolution scenario is not ruled out by the data even though there is an indication of evolution at least at 150 mJy. If this single data point is higher just by chance, no-evolution would be the most obvious match to the data.

When comparing our 90 μm source counts with the HH87 100 μm source counts and the empirically scaled 60 μm counts there seems to be a fairly good agreement between our results and the results obtained by HH87, Bertin et al. (1997), and also the number densities found by Gregorich et al. (1995). It is seen that the curve for our cumulated source counts is flattening below a flux of 150 mJy. This effect might be a result of incompleteness below this level but it could also indicate that the number density of sources below this level is actually leveling out. At the brighter end the number density falls of somewhat more steeply than Bertin et al. (1997) which probably is due to the low probability of finding sources this bright in an area of only a few deg^2. This trend is also seen in the HH87 100 μm number counts.

Puget et al. (1999) and Dole et al. (1999) present results from the FIRBACK survey at 175 μm using the ISOPHOT C200 detector. Puget et al. (1999) discuss the FIR properties of the sources detected in the survey by performing a crude estimate of the number of sources one would expect if the galaxies seen at 175 μm are induced by the low redshift galaxies detected by IRAS at 60 μm. This estimate is based on the IRAS 60 μm galaxy counts as given by Lonsdale et al. (1990) and Bertin et al. (1997) and on a constraint on the color $\frac{f_\nu(175\,\mu\mathrm{m})}{f_\nu(60\,\mu\mathrm{m})} \leq 1.5$ resulting from IRAS, ISO and ground based measurements of a few galaxies classified as starbursts or mergers. Based on the counts for the entire survey as given by Dole et al. (1999) one finds that the extrapolated IRAS counts underpredict the 175 μm counts by a factor of 5.5. As noted by Puget et al. (1999) the ISOPHOT Serendipity Survey which also has gathered data at 175 μm (Stickel et al. 1998) tends to yield a $\frac{f_\nu(175\,\mu\mathrm{m})}{f_\nu(60\,\mu\mathrm{m})} \sim 2$. Using this color ratio the extrapolated 60 μm IRAS counts end up being a factor ~ 2.5 lower than the 175 μm counts. If the number densities found by Gregorich et al. (1995) are used, still employing $\frac{f_\nu(175\,\mu\mathrm{m})}{f_\nu(60\,\mu\mathrm{m})} = 2$, the factor is even further reduced to a factor of about 2. This in turn means that even though we expect the sources found at 175 μm to have a higher median redshift than the sources detected by IRAS there might not be such a large discrepancy in the populations detected as concluded by Puget et al. (1999). This view is further strengthened by very recent observations of FIRBACK sources using SCUBA reported by Scott et al. (1999). Out of 10 bright 175 μm sources 4 objects are convincingly detected at 850 μm and fits to simple spectral energy distributions suggest a range of low to moderate redshifts, $z < 1$. It should also be mentioned that the counts presented by Dole et al. (1999) are well in line with the E-model by Guiderdoni et al. (1998) whereas the model by Franceschini et al. (1998) overpredict the counts at the bright end.

The recent results from submillimeter surveys at 850 μm presented by Blain et al. (2000), Hughes et al. (1998), Barger et al. (1999) and Eales et al. (1999) indicate a number density at a flux level of about 1 mJy which is more than two orders of magnitude higher than would be expected on the basis of a non-evolving local IRAS luminosity function (Smail et al. 1999). The E-model by Guiderdoni et al. (1998) is well in line with the number densities found by Blain et al. (2000), Hughes et al. (1998) and Eales et al. (1999) whereas the counts presented by Barger et al. (1999) are a few times too low compared to this model. The model presented by Franceschini et al. (1998) underpredicts the counts by a factor of a few. As discussed by

Puget et al. (1999) the source counts at 850 μm are more sensitive to the details of evolutionary scenarios, like those discussed by Guiderdoni et al. (1998), than is the case for the counts at 60 μm. The reason for this behaviour is threefold: (1) The rest-frame wavelength range around 100 μm holds the major part of infrared emission due to starformation. (2) The star formation rate increases strongly between $z = 0$ and $z = 1.5$ and a similar behaviour in the infrared is likely. (3) The *negative* k-correction at submillimeter wavelengths favours the detection of high-z objects. Given this the 850 μm counts seem at present to favour the Guiderdoni et al. (1998) E-model including a rapidly increasing fraction of ULIRGs with redshift.

5. Conclusion

Using the ISOPHOT C100 detector we have conducted a deep survey at 60 μm and 90 μm in a small part of Selected Area 57 near the North Galactic Pole. We have produced maps with spatial resolution much higher than IRAS and have established a calibration which is in line with both the COBE DIRBE annual average sky background and IRAS point sources to within about 25% at least at 60 μm.

Source counts based on the combined source detections both in the HUNNSA57 data and our reduction of the Lockman Hole 90 μm survey indicate that evolution as given by the models of Guiderdoni et al. (1998) (E-model) and Franceschini et al. (1994) is consistent with our data. Our data do however not permit us to discriminate between these models and do furthermore not rule out no-evolution scenarios even though there is an indication of evolution at least at 150 mJy. Based on the source counts at 850 μm presented by e.g. Blain et al. (2000) it seems however that the E-model by Guiderdoni et al. (1998) is at present the model best in line with observational evidence at both FIR and submillimetre wavelengths.

Our 90 μm source counts are in line with HH87 100 μm source counts and the empirically scaled 60 μm results from Bertin et al. (1997), HH87 not precluding the number densities found by Gregorich et al. (1995).

In paper II a detailed discussion of the individual sources detected in this survey will be given focusing on optical identification of the sources by means of optical imaging and spectroscopy.

Acknowledgements. The ISOPHOT data presented in this paper were partly reduced using PIA Version 7.3.1(e), which is a joint development by the ESA Astrophysics Division and the ISOPHOT Consortium. We would like to thank Bruno Guiderdoni (IAP, France) and Alberto Franceschini (University of Padova, Italy) for providing us their evolutionary models. Finally we would like to thank the PHOT Instrument Dedicated Team (ESA/VILSPA, Madrid) – especially Bernhard Schulz and Carlos Gabriel – for their help and support.

References

Acosta-Pulido J.A., Schulz B., 1996, CRE non-linearity correction from PV phase calibration report, June 1996.
Ashby M.L.N., Hacking P.B., Houck J.R., Soifer B.T., Weisstein E.W., 1996, ApJ 456, 428
Barger A.J., Cowie L.L., Sanders D.B., 1999, ApJ 518, L5
Bassani L., Dadina M., Maiolino R., et al., 1999, ApJS 121, 473
Blain A.W., Ivison R.J., Kneib J.-P., Smail I., 2000, Galaxy counts at 450 μm and 850 μm. In: Bunker A.J., van Breugel W.J.M. (eds.), The Hy-redshift universe: Galaxy formation and evolution at high hedshift, ASP conference series, vol. 193
Beichman C.A., Neugebauer G., Habing H.J., Clegg P.E., Chester T.J. (eds.), 1985, Infrared Astronomical Satellite (IRAS), Catalogs and Atlases, Explanatory Supplement, GPO, Washington DC
Bertin E., Arnouts S., 1996, A&AS 117, 393
Bertin E., Dennefeld M., Moshir M., 1997, A&A 323, 685
Cohen M., Witteborn F.C., Carbon D.F., et al., 1996, AJ 112, 2274
Dole H., Lagache G., Puget J-L., et al., 1999, FIRBACK far infrared survey with ISO: Data reduction, analysis and first results. In: Cox P., Kessler M.F. (eds.), The Universe as seen by ISO, Vol. 2, SP-427, ESA Publications Division, ESA/ESTEC
Eales S., Lilly S., Gear W., et al., 1999, ApJ 515, 518
Franceschini A., Mazzei P., De Zotti G., 1994, ApJ 427, 140
Franceschini A., Andreani P., Danese, L., 1998, MNRAS 296, 709
Gabriel C., Acosta-Pulido J., Heinrichsen I., Skaley D., Morris H., Tai W.-M., 1997, The ISOPHOT Interactive Analysis PIA, a calibration and scientific analysis tool. In: Hunt G., Payne H.E. (eds.), Proc. of the ADASS VI conference, ASP conference series, vol. 125
Gregorich D.T., Neugebauer G., Soifer B.T., Gunn J.E., Herter T.L., 1995, AJ 110, 259
Guiderdoni B., Hivon E., Bouchet F.R., Maffei B., 1998, MNRAS 295, 877
Hacking P., Houck J.R., 1987, ApJS 63, 311
Hacking P., Condon J.J., Houck J.R., 1987, ApJ 316, L15
Hauser M.G., Kelsall T., Leisawitz D., Weiland J. (eds.), 1997, COBE Diffuse Infrared Background Experiment (DIRBE) Explanatory Supplement, version 2.1, COBE Ref. Pub. No. 97-A, Greenbelt, MD: NASA/GSFC
Herbstmeier U., Ábrahám P., Lemke D., et al., 1998, A&A 332, 739
Hughes D.H., Serjeant S., Dunlop J., et al., 1998, Nat 394, 241
Jourdain de Muizon M., Habing H.J., 1992, The ISO ground-based preparatory programme working group (ISO-GBPPWG). In: Encrenaz Th., Kessler M.F. (eds.), Infrared astronomy with ISO, Les Houches series, Nova science publishers Inc.
Kawara K., Sato Y., Matsuhara H., et al., 1998, A&A 336, L9
Kessler M.F., Steinz J.A., Anderegg M.E., et al., 1996, A&A 315, L27
Klaas U., Krüger H., Heinrichsen I., Heske A., Laureijs R. (eds.), 1994, ISOPHOT Observer's Manual, version 3.1
Koo D.C., Kron R.G., Cudworth K.M., 1986, PASP 98, 285
Lemke D., Wolf J., Schubert J., Patrashin M., 1993, SPIE 1946, 261
Lemke D., Garzon F., Gemünd H.P., et al., 1994, Opt. Eng. 33(1), 20
Lemke D., Klaas U., Abolins J., et al., 1996, A&A 315, L64
Linden-Vørnle M.J.D., 1998, Glitch events in deep ISOPHOT C100 observations: A case study, report
Lonsdale C.J., Hacking P.B., Conrow T.P., Rowan-Robinson M., 1990, ApJ 358, 60
Mann R.G., 1999, Submillimetre source counts: First results from SCUBA. In: de Oliveira-Costa A., Tegmark M. (eds.), Microwave foregrounds, ASP conference series, vol. 181
Moshir M., et al., 1992, Explanatory Supplement to the IRAS Faint Source Survey, Version 2, JPL D-10015 8/92
Pearson C., Rowan-Robinson M., 1996, MNRAS 283, 174
Puget J-L., Lagache G., Clements D.L., et al., 1999, A&A 345, 29
Rowan-Robinson M., Saunders W., Lawrence A., Leech K., 1991, MNRAS 253, 485

Scott D., Lagache G., Borys C., et al., 1999, astro-ph/9910428
Smail I., Ivison R., Blain A., Kneib J.-P., 1999, Deep sub-mm surveys with SCUBA. In: Holt S., Smith E. (eds.,) After the dark ages: When galaxies were young (the Universe at $2 < z < 5$), American Institute of Physics Press
Soifer B.T., Houck J.R., Neugebauer G., 1987, ARA&A 25, 187
Stebbins J., Whitford A.E., Johnson H.L., 1950, ApJ 112, 469
Stickel M., Bogun S., Lemke D., et al., 1998, A&A 336, 116
van der Bliek N.S., Bouchet P., Habing H.J., et al., 1996, The Messenger 70, 28